

Article

On the Efficiency of a Two-Power-Level Flywheel-Based All-Electric Driveline

Johan Abrahamsson *, Janáina Gonçalves de Oliveira, Juan de Santiago, Johan Lundin and Hans Bernhoff

Division for Electricity, Department of Engineering Sciences, Uppsala University, Uppsala 75105, Sweden; E-Mails: janaina.goncalves@angstrom.uu.se (J.G.O.); Juan.Santiago@angstrom.uu.se (J.S); Johan.Lundin@angstrom.uu.se (J.L.); Hans.Bernhoff@angstrom.uu.se (H.B.)

* Author to whom correspondence should be addressed; E-Mail: johan.abrahamsson@angstrom.uu.se; Tel.: +46-18-4715812; Fax: +46-18-4715810.

Received: 13 June 2012; in revised form: 20 July 2012 / Accepted: 26 July 2012 /

Published: 2 August 2012

Abstract: This paper presents experimental results on an innovative electric driveline employing a kinetic energy storage device as energy buffer. A conceptual division of losses in the system was created, separating the complete system into three parts according to their function. This conceptualization of the system yielded a meaningful definition of the concept of efficiency. Additionally, a thorough theoretical framework for the prediction of losses associated with energy storage and transfer in the system was developed. A large number of spin-down tests at varying pressure levels were performed. A separation of the measured data into the different physical processes responsible for power loss was achieved from the corresponding dependence on rotational velocity. This comparison yielded an estimate of the perpendicular resistivity of the stranded copper conductor of $2.5 \times 10^{-8} \pm 3.5 \times 10^{-9}$. Further, power and energy were measured system-wide during operation, and an analysis of the losses was performed. The analytical solution was able to reproduce the measured distribution of losses in the system to an accuracy of 4.7% (95% CI). It was found that the losses attributed to the function of kinetic energy storage in the system amounted to between 45% and 65%, depending on usage.

Keywords: kinetic energy storage; flywheel; electric machine; driveline; electric vehicle; losses

1. Introduction

Electric vehicles are considered to be a promising alternative for future transportation. High efficiency, zero local and low global emissions [1], as well as low noise and the benefit of regenerative braking make them out-compete traditional internal combustion engine (ICE) vehicles in almost all aspects. However, electric vehicles are still lagging in areas such as range and price [2]. The main energy storage in the electric vehicles of today consists of batteries, but vehicles need both energy (to achieve a long range) and power (for acceleration and efficient regenerative braking) to function properly. Batteries cannot be optimized for both power and energy at the same time. The energy density of a battery is inversely proportional to the power density [3]. Thus, there is always a trade-off between the two features. Separating them into two different components allows the system to be optimized for both energy capacity and power handling. The power can be provided by several different components, including batteries, supercapacitors or flywheels [4,5]. In the system described in this article, a flywheel is responsible for the power handling [6,7].

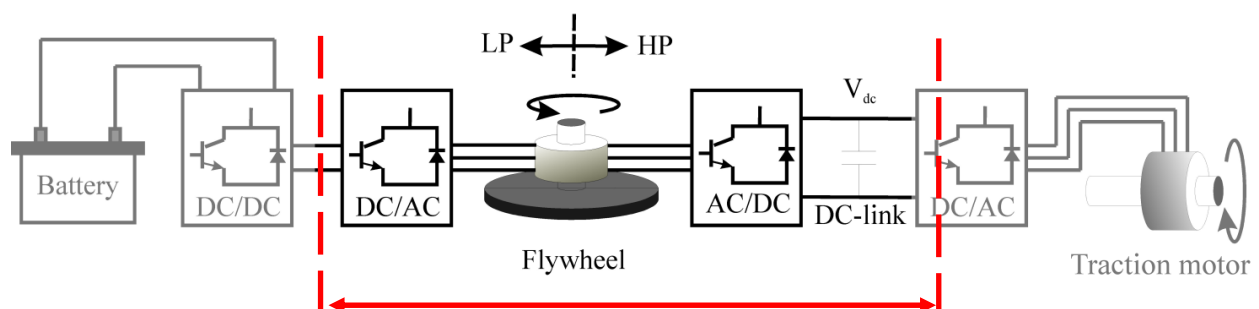
1.1. Description of System

A schematic of the suggested driveline can be seen in Figure 1. A DC/AC converter on the low power (LP) side converts the DC voltage from the energy source to AC voltage, driving the flywheel. Energy can be transmitted from the flywheel to the DC-link via an AC/DC converter on the high power (HP) side, and further delivered to the traction motor.

The flywheel satisfies the transient power demand from the wheel machine, leaving the batteries to be optimized for energy storage. In this way, both power capacity and energy capacity can be optimized. Additionally, the life-time of the battery as well as the efficiency of the complete system can be increased [8].

This article focuses on the losses in the flywheel and the surrounding power electronics, the so called Two-Power-Level-System (TPLS). The power loss in the energy source (e.g., batteries or fuel cells) and the traction motor with driver are therefore not considered.

Figure 1. All-electric driveline based on a double wound flywheel machine. Energy is transferred from the battery to the flywheel at low power. The flywheel delivers/receives high transient power to/from the traction motor. The dotted lines indicate the part of the system (the TPLS) under consideration in this paper.



1.2. Efficiency

Efficiency can be defined in terms of the amount of energy required by a component to achieve a specific goal. In simple systems, it may be sufficient to compare useful output power with the input power. However, for energy storage systems, the most important loss may well be the stand-by loss. Efficiency should then be defined in terms of the losses associated with the storage of a given amount of energy.

It is impossible to describe the overall efficiency with only one number for a complex system such as the Two-Power-Level-System presented in this article. Occasionally the output power in the traction motor is much higher than the input power from the batteries, *i.e.*, the energy stored in the components of the driveline needs to be taken into account. Furthermore, the efficiency is highly dependent on the applied drive cycle, the sizing of the flywheel, and the control strategies chosen.

To create a useful description of system efficiency, the losses in the driveline must be conceptualized by a division into three groups:

1. **Power dependent losses—low power side:** This group consists of losses in the power electronics, but also includes the resistive loss in the low power side windings of the electric machine. Losses are mainly a function of power into the flywheel from the battery.
2. **Energy dependent losses—flywheel:** The loss mechanisms in this group are complex and sometimes interconnected. The losses may be classified as bearing losses, drag losses, eddy current losses and hysteresis losses. A thorough theoretical understanding of the loss mechanisms, both qualitatively and quantitatively, is required to properly analyze measured data. The losses are mainly a function of the rotational speed (amount of stored energy) in the flywheel.
3. **Power dependent losses—high power side:** This group consists of losses in the power electronics, but also includes the resistive loss in the high power side windings of the electric machine. Losses are mainly a function of power from/to the flywheel to/from the wheel motor.

This conceptual division is independent on the physical construction of the system. A detailed analysis of the different losses existent in the system is required to calculate the efficiency for each group, for the flywheel machine, and for the complete driveline.

1.3. Further Applicability

Although this investigation is based around the construction of a driveline for electric vehicles, the concept of efficiency as defined above can be applied in a wider context. In [9], a TPLS for smoothing the output of various systems for generation of intermittent renewable electricity utilizing a kinetic energy storage system was investigated. A rough dimensioning of the sizes of the flywheels was completed. The above conceptualization can be applied to such systems in order to generate a meaningful metric for comparing efficiency. Further, the analytical tools and methods developed in this paper can be applied to analyze the losses in such systems.

2. Method

The efficiency of the system has been investigated both theoretically and empirically. Each physical loss factor has been theoretically analyzed and compared with measurements. The following sections describe the details of the basis for this investigation.

2.1. Experimental Set-up

The system described in Section 1.1 has been implemented in an experimental set-up. A voltage source connected to the grid and supplying constant DC power was used instead of batteries. Furthermore, the shaft of the traction motor was mechanically connected to a secondary electric machine, simulating the resistive torque associated with air friction, rolling friction and inclination of the road.

2.1.1. DC/AC Converter—Low Power Side

The purpose of the power electronics on the low power side was to invert the DC power from the power source into three phase AC power required to drive the flywheel. To this end, one three-phase MOSFET bridge was constructed to achieve vector-control of the flywheel. The switching frequency applied was 20 kHz, and the primary control variable was angular velocity. For more information, see [10]. Detailed description of hardware:

- Microcontroller, dsPIC30F2010 (Microchip);
- Digital angular position sensors, Hall-effect sensors A1101 (Allegro);
- IGBT module, SK22GD123D (Semikron);
- Three-phase bridge driver IR2130 (International Rectifier).

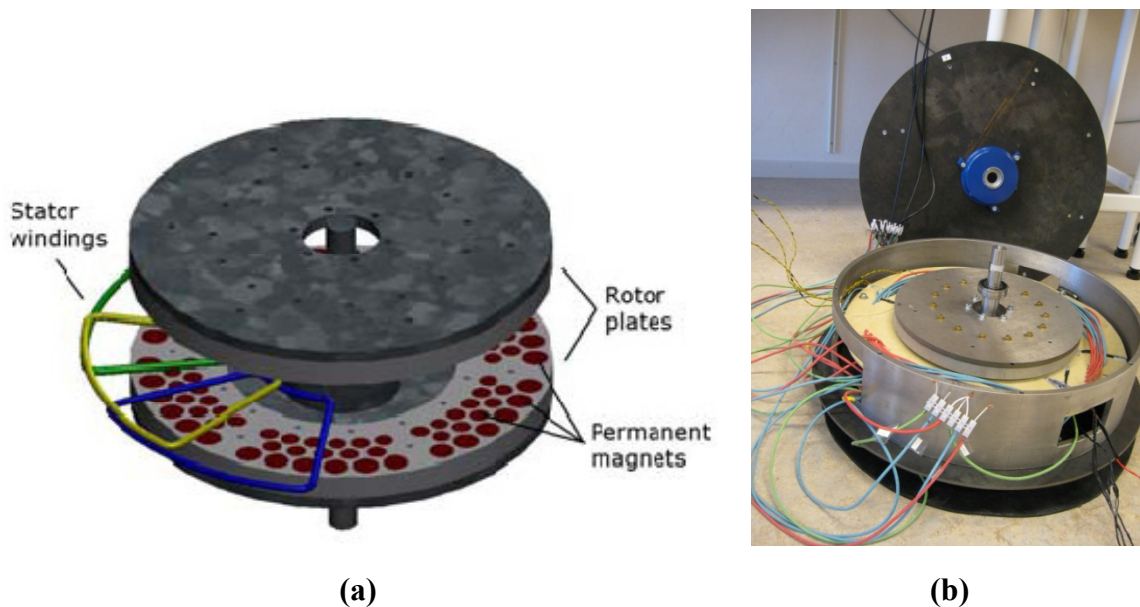
2.1.2. Flywheel Electric Machine

Two sets of electrically insulated three-phase windings with different number of turns were utilized in the electric machine to convert electrical energy to/from kinetic energy of the flywheel. This enabled the flywheel to both receive and provide power independently at two different power levels, independently of each other [11]. The lower power level was connected to the DC source, while the higher power level was connected to the traction motor. The electric machine used was a permanent magnet synchronous machine with axial magnetic flux, see Table 1 and Figure 2.

Table 1. Parameters of the flywheel electric machine.

Parameter	Unit	Low power side	High power side
Nominal speed	rpm		2200
Moment of inertia	kg·m ²		0.364
Friction factor	Nms		0.22
Number of poles	---		6
Internal phase resistance	ohm	0.04	0.12
Internal phase inductance	mH	0.019	0.19
Mutual inductance	mH	0.079	0.076
Magnetic flux	mWb		2

Figure 2. (a) Drawing of the inner part of the axial flux machine under investigation. The complete structure was enclosed in a cylindrical vacuum chamber; (b) Picture of the constructed flywheel machine. The stator windings were attached to a non-conducting epoxy structure.



2.1.3. AC/DC Converter—High Power Side

The purpose of the power electronics on the high power side was to rectify the output from the flywheel and feed/sink the DC-link in such a way that the DC voltage remained constant. To this end, two three-phase MOSFET bridges were built with snubber circuits based on a parallel connection of a filter capacitor and a damping resistor in order to eliminate the ringing presented in the MOSFET output. The control of the converter was achieved using two microcontrollers.

The high power side of the flywheel was connected to a 600 μH inductor on each phase, required for the functionality of the forced-commutated rectifier. A 20 mF, 350 V capacitor was connected across the DC-link.

Current sensors were used to capture the instantaneous values of the AC currents. The hall effect sensors (angular velocity of flywheel) were required for the rectifier control strategy. The encoder was used to estimate the wheel motor rotor angle for the inverter board. The switching frequency was 15 kHz and the primary control variable was DC-link voltage. For more information, see [10].

Detailed description of hardware:

- Piccolo TMDSCNCD28035 microcontroller (Texas Instruments)
- Digital angular position sensors, Hall-effect sensors A1101 (Allegro)
- Current sensors HAL50-S (LEM)
- MOSFET module DSEI 2130 (Semikron)
- Three-phase bridge drivers IR2130 (International Rectifier)
- Optocouplers A4800 (AVAGO).

2.1.4. Measurement System

All measurements were made using a NI CRIO 9022 real time controller, from National Instruments equipped with suitable measurement modules. Five inductive current probes was additionally inserted into the driveline, see Table 2.

Table 2. Description of hardware used for measuring.

Name	Type	Bandwidth	Range	Accuracy	Channels
	n/a	kHz	V	n/a	n/a
NI 9225	Voltage	24.56	300 (RMS)	0.01%	3
NI 9229	Voltage	50	±60	0.20%	4
NI 9205	Voltage	125	±10	0.03%	32
Agilent 1146A	Current	100	±100 (peak)	4% (up to 40 A)	1

Data acquisition rate was set to 10 kHz for both voltage and current measurements. The output of the current probes was logged through the voltage module NI 9205. In this way, it could be ensured that no artificial delay was introduced between measurements of current and voltage.

2.2. Model of Losses—Power Electronics

Power electronics, IGBTs, MOSFETs and diodes, take on various static and dynamic states in cycles when operated as switches. Power is dissipated in any of these states, heating the semiconductor and adding to the total losses of the switch.

At every change of state, if the switch carrying current is opened, a voltage rise occurs across the switch as the current through it falls, resulting in the dissipation of a short pulse of power. Similarly, power is lost as the switch is closed, since the current requires a certain rise-time and the voltage drop is not instantaneous [12].

The average switching power loss, P_S , in the switch due to these transitions can be approximated as [13]:

$$P_S = \frac{1}{2} V_d I_0 f_S (t_{c(on)} + t_{c(off)}) \quad (1)$$

where V_d is the voltage across the switch, I_0 the current flowing through the switch and f_S is the switching frequency. $t_{c(on)}$ and $t_{c(off)}$ are the turn-on and turn-off time of the switch, respectively.

The average power dissipated during the on-state, P_{ON} , is another major contribution to the power loss in the switch. It varies in proportion to the on-state voltage. The on-state losses, or conduction losses, are given by:

$$P_{ON} = V_{ON} I_0 \frac{t_{ON}}{T_S} \quad (2)$$

showing that the on-state voltage, V_{ON} , in a switch should be as small as possible. t_{ON} is the interval in which the switch is conducting and T_S is the switching time period.

The power loss on the LP- and HP-sides, P_{LP} and P_{HP} respectively, could be attributed to these different mechanisms and computed as follows:

$$\begin{aligned}
 P_{LP} &= P_S(IGBT + diodes) + P_{on}(IGBT + diodes) + P_{FW_LP}, \\
 P_{HP} &= P_{ind} + P_S(MOSFET + diodes) + P_{on}(MOSFET + diodes) + P_{FW_HP}
 \end{aligned}
 \tag{3}$$

where P_{FW} is the resistive loss inside the windings of the flywheel machine and P_{ind} are the resistive losses in the inductor.

2.3. Model of Losses—Electric Loss in the Machine

The flywheel electric machine implemented was an axial flux, coreless permanent magnet machine. Insulated copper wires placed in an epoxy structure were used as stator. In this way, the only electromagnetic loss mechanisms occurring in the machine were found to be resistive losses and eddy-current losses in the copper windings. In particular, hysteresis losses were not present since no magnetic steel was used in the construction of the stator.

Further, the two rotor plates with magnetic steel as back yoke ensured a high degree of magnetic confinement. Direct measurements of the stray magnetic field in the region outside the stator yielded values of less than 5 mT, implying that stray losses were negligible.

2.3.1. Resistive Losses in the Copper Windings

Joule losses, P_j , refer to the heating losses produced in the conductors by the line current. These losses depend on the instantaneous amount of power transferred to or from the electric machine, implying a quadratic dependence on current. Considering an electrical wire with constant cross-sectional area A and length l , and assuming further a uniform flow of electric current throughout the conductor, the resistive power loss of the cable may be written as:

$$P_j = \rho_{20}(1 + \alpha\Delta T)\frac{l}{A}I^2 \tag{4}$$

ρ_{20} being the resistivity of the material at 20 °C. The resistivity of the conductor changes with temperature according to the temperature coefficient, α . ΔT is the difference between operating temperature of the conductor and 20 °C.

2.3.2. Eddy Current Losses

Eddy currents on the surface shield the inner part of the conducting material to a certain extent. The skin depth, δ , is a measure of how deep the currents penetrate into the conductor. It is defined as the depth at which the magnitude of the induced current density has fallen to $1/e$ (approximately 37%), where e is Euler's number. For good conductors at relatively low frequencies, the skin depth may be approximated as:

$$\delta = \sqrt{\frac{2 \cdot \rho}{\omega_e \cdot \mu_0 \cdot \mu_r}} \tag{5}$$

where ρ is the resistivity of the material, ω_e the angular frequency of the time varying electromagnetic field, μ_0 the permeability in vacuum and μ_r the relative permeability.

The skin depth in copper at 150 Hz is approximately 5 mm. The coils in the electric machine were wound using multi strand conductors with a radius much smaller than the skin depth. It was therefore assumed that the time varying magnetic field completely penetrated the conductors. The eddy current losses, P_e , may in this case be obtained using the analytic expression:

$$P_e = C_E \omega_e^2 = \frac{d^2 \omega_e^2 V}{32 \rho_t} \sum_i^n B_p^2(i) i^2 \quad (6)$$

where d is the diameter and V the total volume of the conductors. $B_p(i)$ is the peak flux density of the i :th harmonic and ρ_t the resistivity of the conductor perpendicular to its length, [14]. The eddy current loss decreases with the square of the diameter of the insulated conductors for a given active volume. Note that since oxidation layers form on the surface of the individual strands in a multi-stranded lead, it is imperative to take into account the interstrand resistivity in order to calculate the resulting eddy-current losses. This resistivity may differ significantly from the resistivity of pure copper [15].

2.4. Model of Losses—Bearings

The very high rotational speed required to achieve a high specific energy of the complete system leads to large mechanical losses in the bearings. The first really thorough treatise on the topic was written by Alfred Palmgren of ABSKF in 1959, [16], based on [17]. It was shown that the power loss in the bearing could be divided into two parts, one dependent on load and one on the viscous friction of the lubricant. The part due to the loading of the bearing was found to increase linearly with rotational speed, while the part depending on viscous friction was found to increase as rotational speed to the power of 5/3 for moderate to high rotational speeds:

$$\begin{aligned} P_{load} &\propto n, \\ P_{visc} &\propto n^{5/3}, \quad \nu n \geq 2000 \end{aligned} \quad (7)$$

where ν [mm²/s] is the kinematic viscosity of the lubricant and n [rpm] the rotational speed.

Further investigation showed that a more accurate description of frictional torque is obtained by basing the division on the source of the losses. In modern bearing analysis, the mechanical power loss from a ball bearing, P_b , can be described by the following equation:

$$P_b = P_{rr} + P_{sl} + P_{seal} \quad (8)$$

where P_{rr} is the rolling power loss, P_{sl} the sliding power loss and P_{seal} the frictional power loss from the seals in case of a sealed bearing. Sealed bearings are used in low pressure environments to keep the lubrication from evaporating. A detailed description of the different loss mechanisms can be found in [18]:

- **Rolling power loss** is caused by rolling contact friction as the balls in the bearing roll over the raceways. It occurs partly due to a sliding motion induced by the deformation of the balls in the bearing as well as the raceway, and partly due to mechanical hysteresis as the metal parts deform and regain their shape. The rolling power loss depends on the kinematic viscosity, which in turn depends on the type of lubricant used in the bearing and on operating temperature. The viscosity typically varies with at least one order of magnitude over a temperature span of 60 °C.

- **Sliding power loss** is mainly caused by sliding friction between the rolling elements of the bearing, *i.e.*, surface to surface contact of the balls in the raceway, and from the contact between the balls and the guiding surfaces of the cage of the bearing. It depends on the sliding friction coefficient, μ_{sl} , normally assumed to be constant.
- **Power loss due to seals** is caused by the friction occurring as the seals of the bearings slide against the rotating part. The eccentricity of the rotor has an insignificant effect on this power loss, since the absolute displacement of the inner rim of the bearing compared with the outer rim is small. The resulting compression of the seal results in a minor increase of pressure on the rim from the rubber, due to its high elasticity.

A summary of the analytical description of each loss mechanism can be found in Table 3.

Table 3. Analytical description of power-loss in sealed ball bearings.

Loss mechanism	Primary equation (rotational speed)	Auxiliary parameter (geometry and load)
Rolling loss	$P_{rr} = \frac{G_{rr}}{1000} \left(\nu \frac{30\omega_m}{\pi} \right)^{0.6} \omega$	$G_{rr} = R_1 d_m^{1.96} \left(F_r + \frac{R_2}{\sin \alpha_F} F_a \right)^{0.54}$
Sliding loss	$P_{sl} = \frac{G_{sl} \mu_{sl}}{1000} \omega_m$	$G_{sl} = S_1 d_m^{-0.145} \left(F_r^5 + \frac{S_2 d_m^{1.5}}{\sin \alpha_F} F_a^4 \right)^{1/3}$
Seal loss	$P_{seal} = \frac{K_{s1} d_s^\beta + K_{s2}}{1000} \omega_m$	

R_1, R_2, S_1 and S_2 are geometrical parameters, unique for each bearing type. d_m is the average diameter of the bearing in millimeter and ω_m the mechanical angular velocity of the rotor [rad/s]. The angle α_F is further defined by:

$$\alpha_F = 0.429 \left(\frac{F_a}{C_0} \right)^{0.24} \tag{9}$$

where C_0 is the basic static load rating of the bearing, see [19].

F_r and F_a is the radial and axial load on the bearing respectively. In a vertically placed flywheel no external radial load is applied to the rotor. The main radial load is therefore typically created by rotor imbalance. The unbalanced rotor adds a cyclic, radial load to the bearing which can be approximated by [20]:

$$F_r = m e_r \omega_m^2 \tag{10}$$

where m is the total mass of the rotating part, and e is the distance between the mass center and the axis of rotation.

To conclude: the rolling loss in the bearing is in general a function of rotational speed to the power of 1.6, caused by the axial load. However, eccentricity in the rotor, causing a dynamic radial force on the bearing, generates a component of loss corresponding to the rotational speed to the power of 2.68.

Similarly, the power loss associated with the sliding motion of the rolling elements depends in general linearly on the rotational speed, caused by the axial load. However, also here the eccentricity of the rotor causes a component proportional to the angular velocity to the power of 4.33.

Finally, the losses associated with the rubber seal of the bearing depend linearly on the rotational speed. The frictional torque from the seals is normally the largest component of power loss at moderate angular speeds. However, the rubber in the seal may change shape significantly during the life of the bearing, due to wear or environmental conditions. A direct measurement of the frictional torque due to the seals may be required in order to validate the theoretical formula.

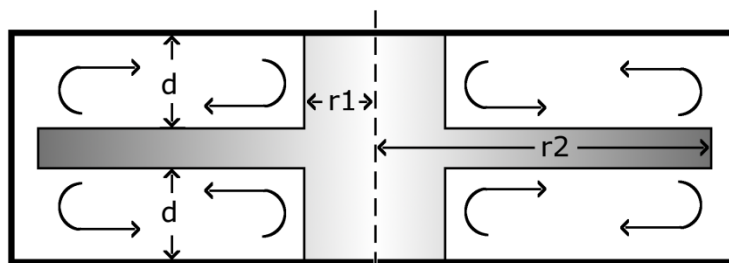
2.5. Model of Losses—Drag

One of the dominant loss mechanisms in high-speed machines results from drag on the surface of the rotor. An accurate description of the loss as a function of air pressure is important in order to determine the level of vacuum required to limit frictional loss.

2.5.1. Enclosed Disc

An estimation of the loss can be made by approximating the geometry of the rotating part of the axial flux electric machine as discs. Each disc is enclosed in its own cylindrical container. The quota between the axial distance from the disc to the enclosure, and the outer radius of the disc determines the topology of the flow inside the machine. This quota is called the *spacing ratio*, see Figure 3.

Figure 3. Schematic picture of a disc rotating inside a cylindrical enclosure. The arrows describe the radial mass transport occurring in the turbulent flow regimes. Of particular interest is the ratio d/r_2 , called the *spacing ratio*.



The power loss experienced by a disc inside a cylindrical enclosure can be written as:

$$P_{air} = k_f M_{disc} \omega_m, \quad (11)$$

where M_{disc} is the friction torque on the surface of a smooth, thin rotating disc and k_f a dimensionless roughness factor (1 for a completely smooth disc). The frictional loss between the circumference of the disc and the cylindrical part of the enclosure is ignored. Roughness factors reported in literature are listed in Table 4.

Table 4. Values of k_f , measured empirically and reported in literature.

Source	k_f
Theodorsen and Regier [21]	2–4
Larjola <i>et al.</i> , [22]	2.5
Design of rotating electrical machines [23]	1–1.4

2.5.2. Friction Coefficient

The friction torque on a rotating disc can further be calculated by the equation:

$$M_{disc} = \frac{C_f \rho_a \omega_m^2 (r_o^5 - r_i^5)}{2} \quad (12)$$

where ρ_a is the density of air, r_i and r_o the inner and outer radii of the disc respectively, and C_f the so called *friction coefficient*. For a thorough theoretical discussion, see [24].

The friction coefficient depends to a large extent on the flow pattern generated between the rotor and the enclosure. Four such patterns, or *regimes*, have been identified in literature [25]. A summary of the equations governing the friction coefficient in each of these regions can be found in Table 5.

Table 5. Overview of the possible flow configurations that may occur when a disc rotates inside a cylindrical enclosure.

Regime	Description	C_f (best empirical)
I	Laminar flow, small gap; Merged boundary layers	$C_f = \frac{2\pi}{(d/r_2)R_e}$
II	Laminar flow, large gap; Separate boundary layers with constant velocity core	$C_f = \frac{3.70(d/r_2)^{1/10}}{R_e^{1/2}}$
III	Turbulent flow, small gap; Merged boundary layers, radial mass transport	$C_f = \frac{0.08}{(d/r_2)^{1/6} R_e^{1/4}}$
IV	Turbulent flow, large gap; Separate boundary layers with radial mass transport No radial mass transport in core	$C_f = \frac{0.102(d/r_2)^{1/10}}{R_e^{1/5}}$

where R_e is the so called *tip Reynolds number*, the Reynolds number of a disk rotating in free space, defined as:

$$R_e = \frac{\rho_a \omega_m r_o^2}{\mu}, \quad (13)$$

and μ is the dynamic viscosity of air.

Regime I and III are characterized by a small airgap between the rotating and static surface. The small airgap makes it possible to approximate the flow between the rotating and static surfaces as homogenous, either laminar or turbulent. For the large gaps typically found in electrical machines, separate boundary layers are formed (regime II and IV). Between the layers, there is a core with approximately constant velocity. The laminar boundary layers of region II turn turbulent at higher rotational velocities, *i.e.*, Reynolds numbers.

3. Results

A large number of measurements were made in order to confirm the theoretical framework developed in the previous sections, as well as calculating the efficiency of the constructed driveline. Two different types of tests were performed:

1. **Spin-down tests at varying degrees of vacuum.** The flywheel was accelerated to its maximum velocity, and allowed to spin-down due to internal losses. This test was performed in order to measure drag, bearing friction and eddy-current loss.
2. **Full power test.** The flywheel was accelerated to its nominal speed, and energy was thereafter transferred throughout the complete driveline. This test was performed to measure the efficiency of the power electronics.

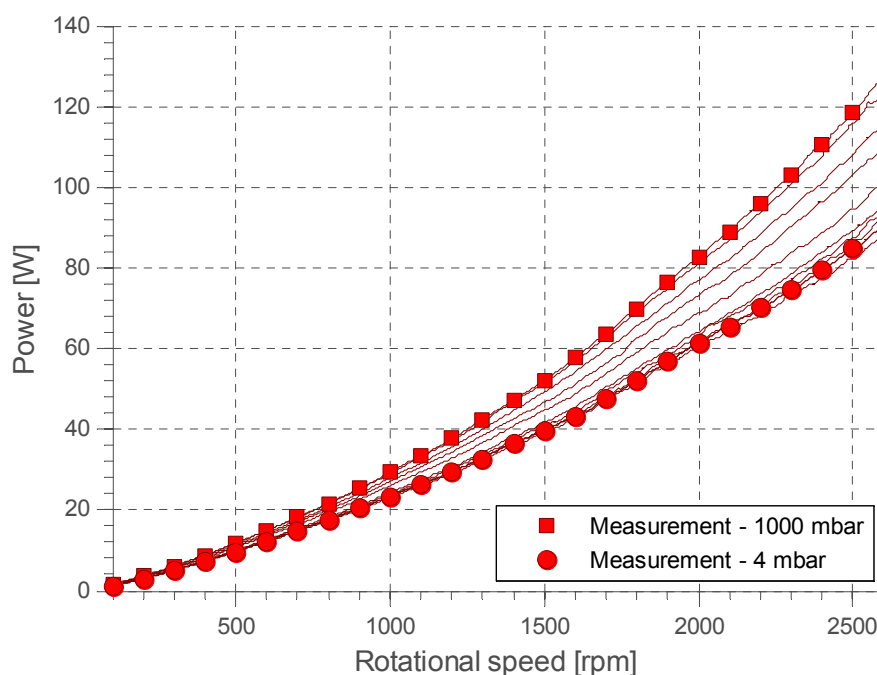
3.1. Spin-Down Tests

A spin-down test is performed by accelerating the motor to its peak rotational speed, disconnecting the power supply and load, and allowing the rotor to spin down due to internal losses. This test was performed several times under varying levels of vacuum in order to calculate the losses associated with the total amount of energy stored in the flywheel. The open-circuit line-to-line voltage induced in the windings on the low power side was recorded continuously during the tests. The frequency of this voltage was then used to calculate the instantaneous mechanical speed, which in turn was used to calculate the total amount of kinetic energy, E_K , stored in the flywheel, using the formula:

$$E_K = \frac{1}{2} I \omega_m^2 \quad (14)$$

where I is the moment of inertia of the flywheel and ω_m is the angular velocity of the rotor. As a consequence, the total instantaneous power loss from mechanical friction, eddy currents and drag could be calculated through derivation of the kinetic energy with respect to time, see Figure 4.

Figure 4. Measurement of power loss during spin-down test. The instantaneous power loss was estimated by numerical derivation of the stored kinetic energy with time. The higher losses correspond to higher pressures. The upper limit correspond to a pressure of 1000 mbar (atmospheric pressure), and the lower limit to 4 mbar.

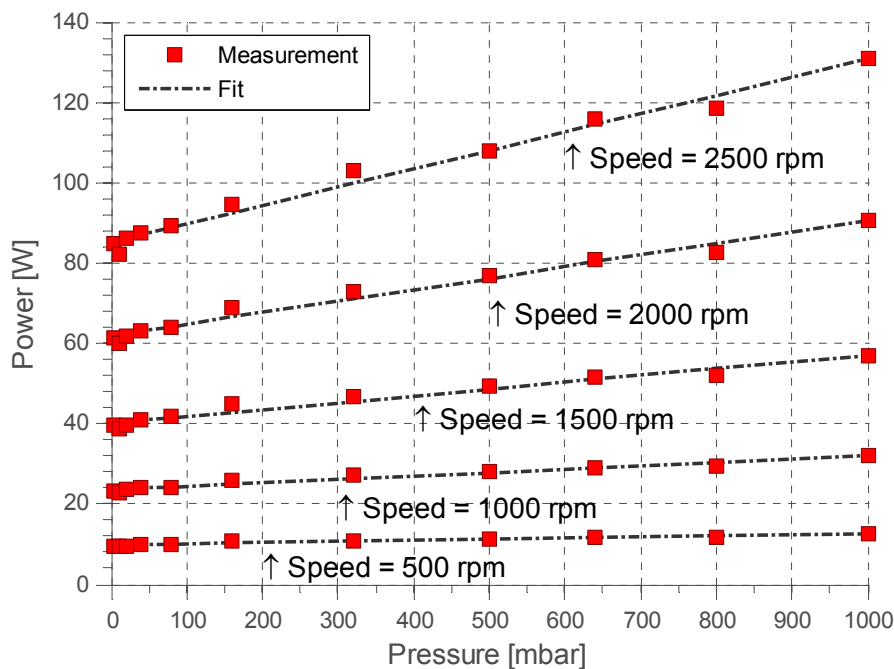


The measurement comprised the sum of drag, eddy-current loss and bearing loss. In order to verify the theoretical models, it was necessary quantify the impact of each loss mechanism individually. The first step to this end was to extract the losses due the drag.

3.1.1. Air Friction

By varying the level of vacuum in the chamber, and measuring the power loss over rotational speed, the effect of drag was quantified. The minimum pressure reached was 4 mbar. By extrapolating the results down to 0 mbar, the total loss due to air friction was estimated, see Figure 5. The drag losses were found to scale linearly with the density of the air, as expected from Equation (12).

Figure 5. Air friction loss over pressure. Note the linear dependence of power loss on air density.



The geometry of the electric machine can be seen in Figure 6. It was assumed that no gas flows axially between the different sections. The machine could under this assumption be modelled as two separate discs, contained in cylindrical enclosures.

According to Equations (11) and (12), the power loss due to air friction became:

$$P_{air} = k_f \frac{\rho_a \omega_m^3}{2} [C_{f1}(r_o^5 - r_{i1}^5) + C_{f2}(r_o^5 - r_{i2}^5)] \tag{15}$$

where C_{f1} is the friction coefficient for the disc with axial clearance d_1 and C_{f2} the friction coefficient for the disc with axial clearance d_2 . The difference in axial clearance caused a difference in friction coefficient for the same rotational speed even though the surface roughness was assumed to be equal.

Further, an estimation of the different flow regimes occurring in the motor was required in order to estimate the two friction coefficients. The parameters used in the calculation of the power loss for the two discs can be found in Table 6.

Figure 6. The power loss due to air friction can be estimated by approximating the shape of the rotor as two discs enclosed in cylindrical boxes. The arrows illustrate the radial mass transport associated with the turbulent flows found in regimes II and IV.

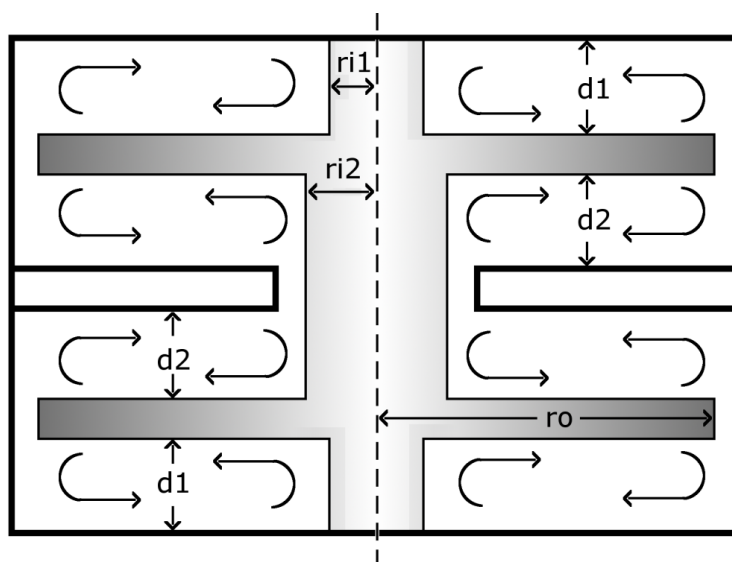


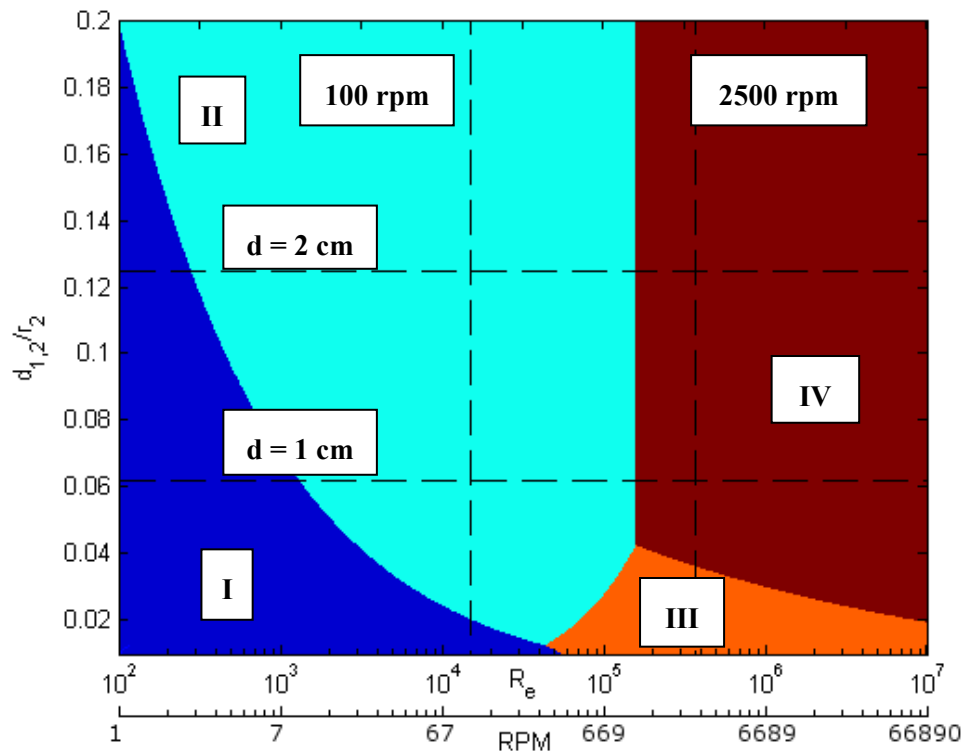
Table 6. Parameters used in the calculation of power loss due to air friction.

Symbol	Parameter	Unit	Value
ρ_a	Density of air	kg/m ³	1.2
μ	Dynamic viscosity	Ns/m ²	19.6×10^{-6}
r_{i1}	Inner radius of rotor	m	15×10^{-3}
r_{i2}	Inner radius of rotor	m	47.5×10^{-3}
r_o	Outer radius of rotor	m	165×10^{-3}
d_1	Axial gap for rotor 1	m	10×10^{-3}
d_2	Axial gap for rotor 2	m	20×10^{-3}

These parameters, together with those in Table 5, were used to generate a theoretical plot of the different flow regimes occurring in the motor as function of Reynolds number and spacing ratio, see Figure 7. The horizontal lines mark the impact of the axial gap distance for the two discs. The vertical lines mark the actual region of operation.

The plot shows that the discs were operating in regime I, corresponding to a situation with laminar flow and merged boundary layers, for very low speeds. However, both discs had already transitioned into regime II at 10 rpm, meaning predominantly laminar flow but with separated boundary layers. Approximately around 1000 rpm, the discs continued into regime IV, a region with turbulent flow and separated boundary layers. The system never entered into region III, corresponding to turbulent flow and merged boundary layers.

Figure 7. Theoretical flow regimes as function of Reynolds number (rotational speed) for the constructed geometry. The transition from region II to region IV was found to take place at a rotational velocity of around 905 rpm for spacing ratios higher than 0.05.



From this it could be concluded that regime II and IV were responsible for the majority of the drag losses. The corresponding friction coefficients were:

$$\text{Regime II: } C_f = \frac{3.70(d/r_o)^{1/10}}{R_e^{1/2}}, \text{ Regime IV: } C_f = \frac{0.102(d/r_o)^{1/10}}{R_e^{1/5}}. \tag{16}$$

The transition from regime II to regime IV occurred when the friction coefficients of the two regimes were equal, leading to a Reynolds number of:

$$R_e^T = \left(\frac{3.70}{0.102} \right)^{10/3} \approx 158000. \tag{17}$$

This transition Reynolds number was in this case independent on the spacing ratio, and so corresponded to a rotational velocity of 905 rpm for both discs.

The total power loss due to air friction in the system could now be calculated by:

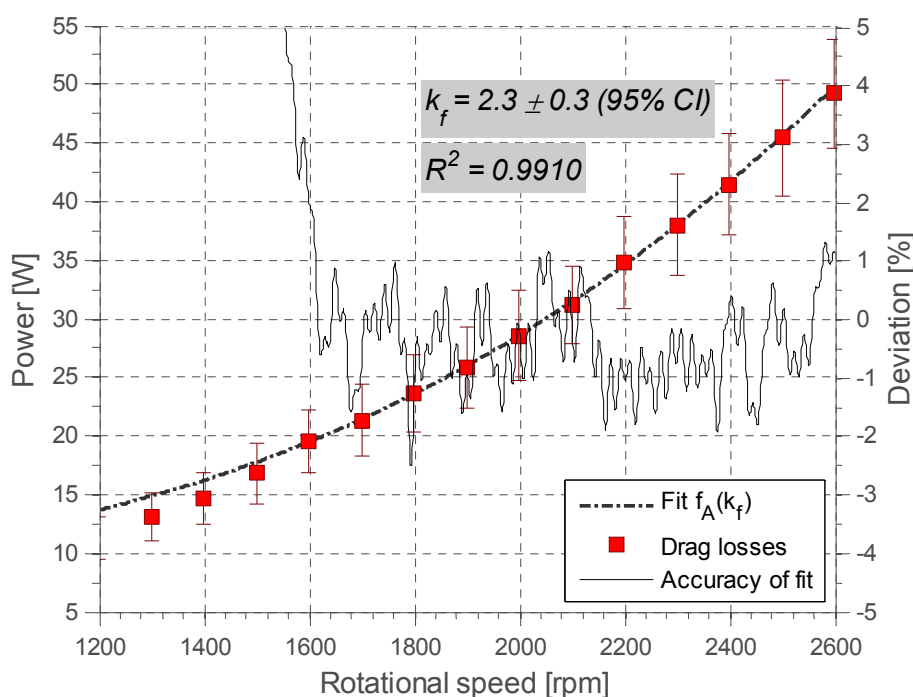
$$\begin{aligned} P_{air} &= k_f \frac{\rho_a \omega_m^3}{2} \left((r_o^5 - r_{i1}^5) \left(\frac{d_1}{r_o} \right)^{1/10} + (r_o^5 - r_{i2}^5) \left(\frac{d_2}{r_o} \right)^{1/10} \right) \frac{3.70}{R_e^{1/2}} \quad R_e < 158000 \\ P_{air} &= k_f \frac{\rho_a \omega_m^3}{2} \left((r_o^5 - r_{i1}^5) \left(\frac{d_1}{r_o} \right)^{1/10} + (r_o^5 - r_{i2}^5) \left(\frac{d_2}{r_o} \right)^{1/10} \right) \frac{0.102}{R_e^{1/5}} \quad R_e \geq 158000 \end{aligned} \tag{18}$$

with:

$$\text{Re} = \frac{\rho_a \omega_m r_o^2}{\mu} \quad (19)$$

However, to fully quantify the power loss due to air friction, the surface roughness factor, k_f , needed to be determined. It was evaluated by comparing the theoretical power loss with the measured one in regime IV (over 1200 rpm), see Figure 8. In this evaluation, the theoretical values were forced to coincide with the measured values at a rotational speed of 2600 RPM.

Figure 8. Measured power loss due to air friction at 1 bar. A roughness factor of 2.3 ± 0.3 was required in order to reproduce the measured values,



The fit of measured power loss together with the analytical analysis revealed that the surface roughness factor amounted to 2.3 ± 0.3 . This was found to correspond well with previously reported values, see Table 4.

After having fully quantified the losses due to drag, the next step of the analysis was to separate the remaining losses from each other. No direct measurement of these individual loss components was possible. Instead, the theoretical background for each loss mechanism was used to extract the components of the loss-curve belonging to signals with different dependencies on rotational speed.

3.1.2. Detailed Analysis of Bearing Loss

The geometry of the electric machine and position of the ball bearings can be seen in Figure 9. The machine was constructed in such a way that the bottom ball bearing supported the complete axial load of the rotor. It was further assumed that the radial load was divided equal between the upper and lower bearings.

The bearings used were of the SKF 6205-2RSH type, sealed for life and lubricated with a mineral oil-based grease—LGMT 2. Thermal measurements in the bearing region showed that the temperature

in the region of the bearings was approximately $60\text{ }^{\circ}\text{C} \pm 10\text{ }^{\circ}\text{C}$, corresponding to a range of kinematic viscosity from $60.5\text{ mm}^2/\text{s}$ to $93.5\text{ mm}^2/\text{s}$, with an average of $77\text{ mm}^2/\text{s}$. The required properties of these bearings can be found in Table 7.

Figure 9. Geometry of the electric machine and position of the ball bearings.

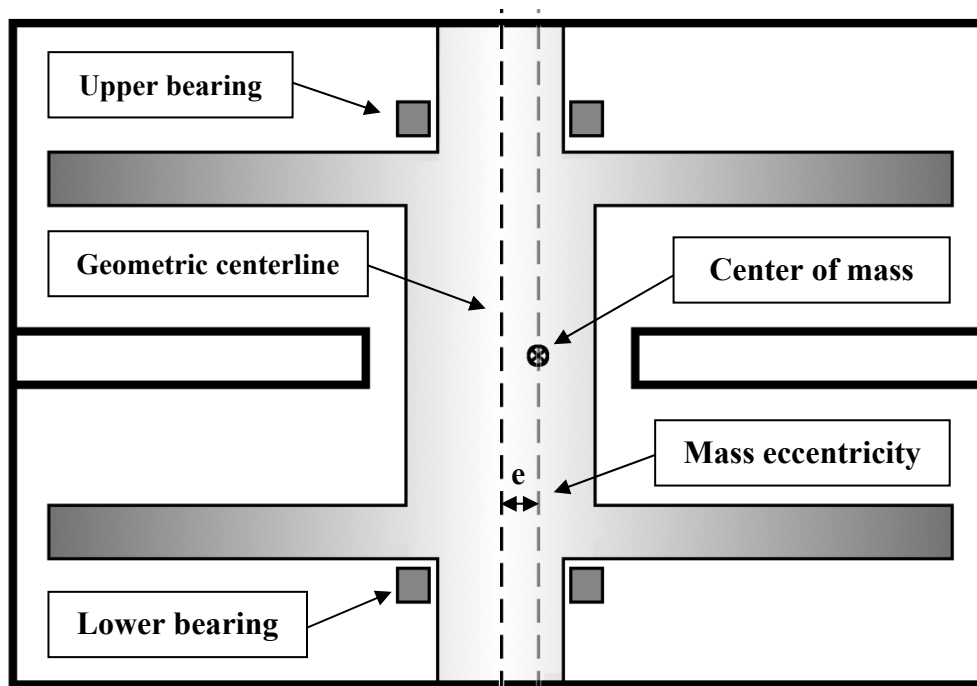


Table 7. Parameters used in the calculation of power loss due to mechanical bearings. All parameters for a given bearing geometry and lubrication can be found in [19] and [26].

Symbol	Parameter	Unit	Value
ν	Kinematic viscosity of grease	mm^2/s	60.5–93.5
F_a	Axial force on lower bearing	N	191
C_0	Basic static load rating	N	7800
μ_{sl}	Sliding friction coefficient	n/a	0.05
d_m	Average bearing diameter	mm	38.5
R_1, R_2	Geometry constants, rolling	n/a	3.9×10^{-7} , 1.7
S_1, S_2	Geometry constants, sliding	n/a	3.23×10^{-3} , 36.5
K_{S1}, K_{S2}, β	Geometry constants, seal	n/a	0.028, 2, 2.25
d_s	Seal counter-face diameter	mm	31.8
τ_{seal}	Measured seal friction	Nmm	72

Direct measurements of the frictional torque from the seals of the bearings were performed. The measurements indicated that each bearing was exposed to an approximate torque of 72 Nmm. This value deviated significantly from the nominal value of 82.2 Nmm, calculated from geometry according to Table 3. The measured value was used in the further analysis.

The only remaining unknown factor impacting the losses in the bearing was the rotor imbalance, e_r . The imbalance of the rotor was therefore left as a free parameter, to be estimated from the measurements.

3.1.3. Detailed Analysis of Eddy Current Loss

The magnetic field passing through the windings from the permanent magnets in the rotor induces eddy-currents in the copper wire. This field was calculated with a static 3D FEM simulation. The amplitudes of the harmonics of the magnetic field were found by applying the Fourier transform to the result. The results showed that the first three odd harmonics were responsible for 99% of the total eddy current loss.

Using Equation (6), the results of the FEM simulations and the physical parameters of the winding found in Table 8, a numerical estimate of the eddy current losses could be found.

Table 8. Parameters of the windings of the flywheel electric machine.

Parameter	Unit	Low power side	High power side
Number of phases	n/a	3	3
Number of turns per phase	n/a	12	4
Strands per conductor	n/a		56
Diameter of strands	mm		0.3
Diameter of conductor	mm		2.2
Active length of conductor	m		10.1
Peak B-field	T	1st: 0.420, 3rd: 0.0742, 5th: 0.007	

The numerical estimate resulted in:

$$P_e = \frac{1.32 * 10^{-12}}{\rho_t} \omega_e^2 \quad (20)$$

The remaining unknown factor was the transversal resistivity of the conductor. It was left as a fit-parameter, to be estimated from the measurements.

3.1.4. Estimating the Fit-parameters

After removing the extrapolated drag loss at zero pressure from the measurements, the sum of mechanical and eddy current losses remained from the measurements. Of these remaining losses the electrical losses increased as the square of the rotational velocity, as shown in Section 2.3. The mechanical losses had a more complex dependency, with a strong linear component as well as several nonlinear ones.

By using the theoretical framework describing the rotational dependence of the losses, the two unknown parameters e_r and ρ_t could be estimated. This was achieved by minimizing the difference between the measured and simulated total loss, using the method of least squares. A plot of the correspondence between total measured loss and the sum of the simulated losses according to the above criteria can be found in Figure 10.

The parameters evaluated to $e_r = 2.2 \times 10^{-4} \pm 5.6 \times 10^{-4}$ and $\rho_t = 2.5 \times 10^{-8} \pm 3.5 \times 10^{-9}$. After obtaining these estimations on imbalance and resistivity, the complete decomposition of the measured losses in their individual components could be plotted, Figure 11.

Figure 10. Fit of calculated to measured total power loss using the least squares method, by varying two parameters(e_r and ρ_t) corresponding to mechanical imbalance and perpendicular resistivity of the conductors.

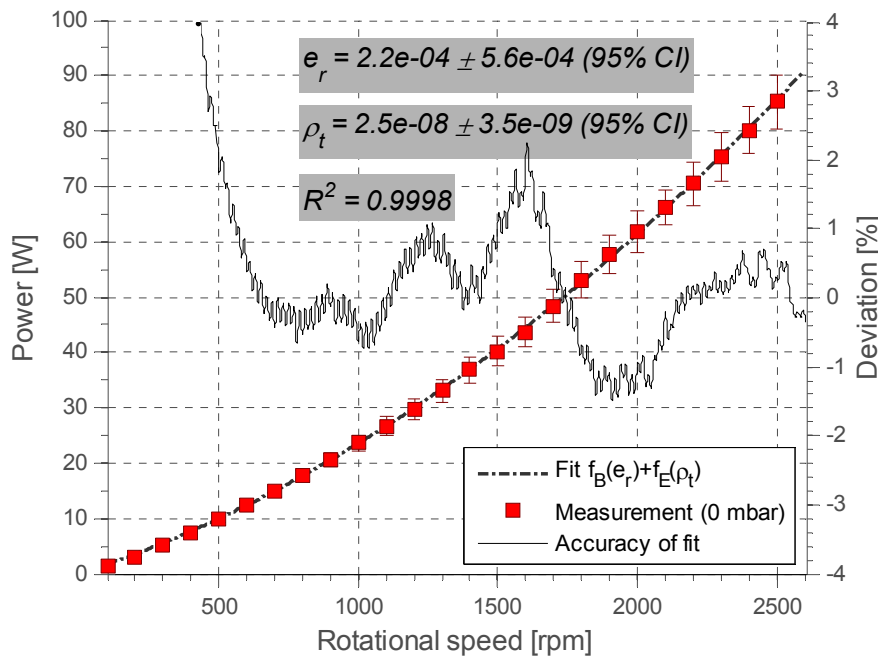
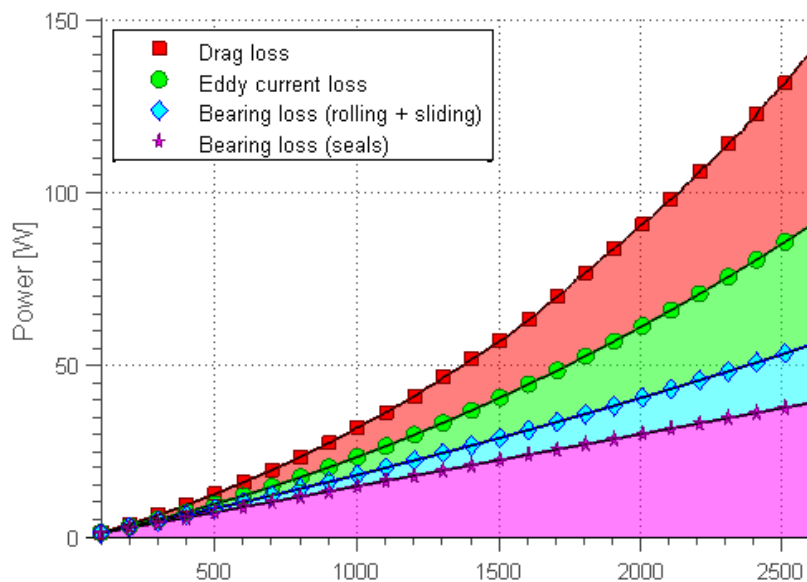


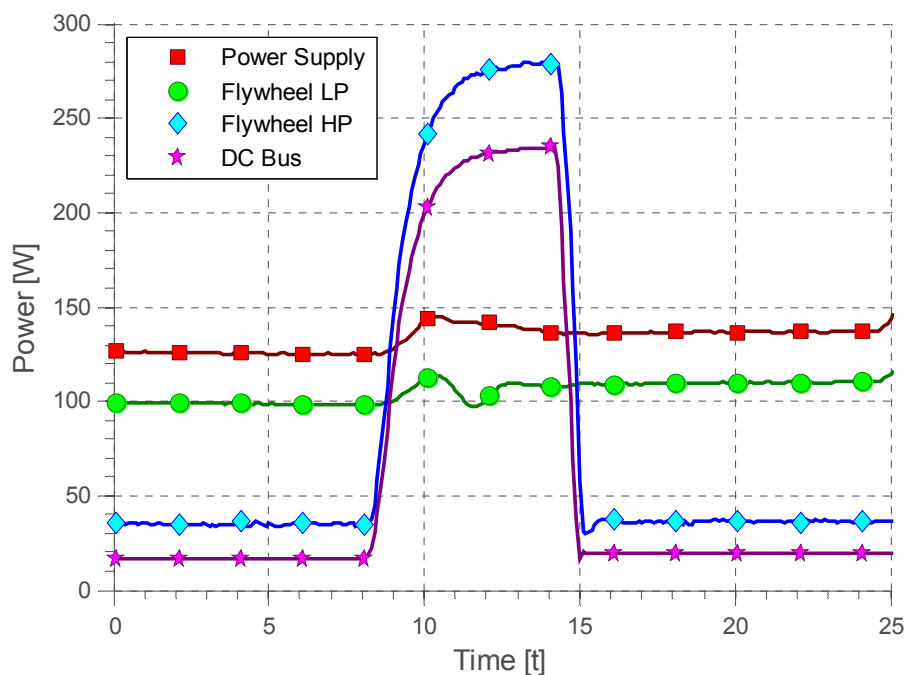
Figure 11. Decomposition of power loss using the dependence on rotational speed.



3.2. Driveline Losses

3.2.1. Power Electronics—Experiment

A number of tests were performed on the driveline for varying input/load powers. The results were used to study the efficiency of the LP and HP sides under various conditions. An example of a test sequence can be found in Figure 12.

Figure 12. Measurement of power in the driveline during a peak power event.

The plot shows the flux of energy delivered from the main power supply, over the flywheel, and finally out from the DC bus into the traction motor. It represented a situation in which the traction motor needed a larger amount of power for a short period of time. This energy was supplied by converting kinetic energy in the flywheel to electrical, while the power supply maintained a more or less constant influx of energy. The efficiencies from power supply to flywheel, and from flywheel to DC-link were computed according to the values presented in Figure 12 during the peak power event ($15 < t < 25$ s).

The powers in the system was evaluated by measuring DC current and voltage after the power supply and out from the DC-link. Measurements were additionally made on the line-to-line-voltages and phase currents of the LP-side of the flywheel as well as the HP-side. All measurements were recorded with a bandwidth of 10 kHz. The results from the evaluation are presented in Figures 13 and 14. Each marker represents the evaluation of one individual peak power event. Notice that the efficiency increases with the power in both cases.

The efficiencies obtained for the HP side are slightly lower than the efficiencies found in the LP side for the same amount of base power. The reason for the lower efficiency is due to the additional losses occurring in the boost circuit of the active rectifier between the flywheel and the DC-link. However, as the transmitted power increases, so does the efficiency. Maximum efficiency was found to be 85% on both high-power and low-power sides.

Figure 13. Efficiency of the LP side of the driveline *versus* the input power, *i.e.*, battery output power.

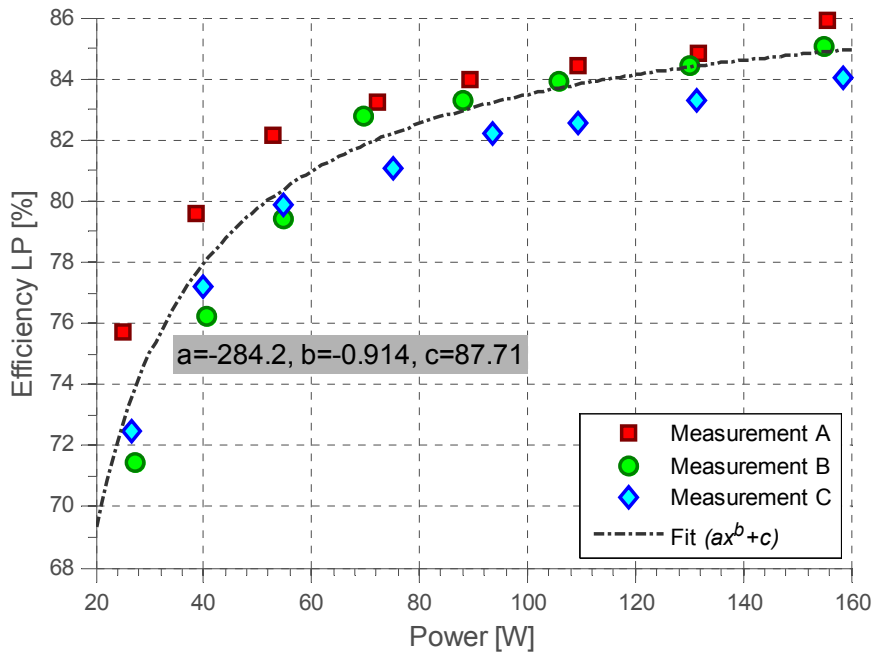
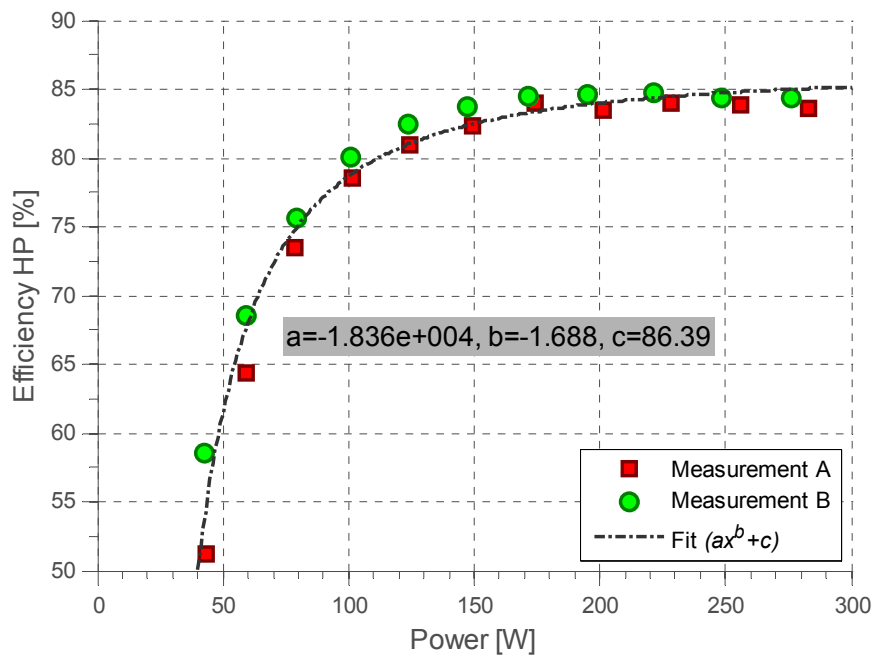


Figure 14. Efficiency of the HP side of the driveline *versus* the load power, *i.e.*, power delivered from the DC-link.



3.2.2. Losses in the Different Components

A Matlab model using the theoretical framework described in Sections 2.2 to 2.5 was implemented. The model computed the losses in the different components of the driveline for a specific operating point. The evaluation of total losses was grouped in LP side components, HP side components and flywheel machine, according to the conceptual groups defined in Section 1.2.

Using this mathematical model, the losses attributed to the different components of the driveline (from DC voltage source on the LP side to DC link on the HP side) were estimated and compared with measurements. Nine test-cases were chosen so as to adequately represent the span of the driveline. The parameters used in both simulation and experiments can be found in Table 9.

The results obtained from the simulation were compared to experimental results. A comparison of the percentages of the distribution of losses according to measurement and simulation can be found in Table 10.

Table 9. Parameters used in measurement and simulation of complete driveline

Parameter	Unit	Value
Power Supply DC voltage	V	35
DC-link voltage	V	100
Flywheel speed	rpm	1,800

Table 10. Comparison of measured and calculated distribution of losses in the system.

Part of driveline	Unit	Test number								
		1	2	3	4	5	6	7	8	9
Measured loss—LP	%	19.2	19.8	24.2	25.0	24.3	23.4	27.5	17.8	31.0
Simulated loss—LP	%	17.2	18.1	20.3	23.1	22.4	20.3	25.7	16.1	28.4
Measured loss—Flywheel	%	63.2	62.7	59.8	50.6	54.9	57.7	47.3	50.3	45.4
Simulated loss—Flywheel	%	64.8	62.2	59.4	50.6	52.0	55.2	46.2	51.0	44.9
Measured loss—HP	%	17.6	17.5	15.9	24.4	20.8	19.0	25.1	31.8	23.6
Simulated loss—HP	%	18.0	19.7	20.3	26.3	25.7	24.5	28.0	32.9	26.7

The flywheel machine was responsible for a major part of the losses, between 45% and 65%, which could be attributed to the mechanical losses in the bearings and the eddy currents created in the windings. For higher levels of transmitted power, the part of the losses occurring in the power electronics increased. Simulation and experimental results were found to be in good agreement. The simulations were able to reproduce measured distribution with an accuracy of 4.7% (95% CI).

4. Conclusions

This paper presents experimental results on a novel electric driveline using a kinetic energy storage module as a means to separate energy storage from power handling. The study found that the losses in the system may be analyzed by separating the complete driveline into three different conceptual parts—the low power side, the flywheel and the high power side. The losses in the low power and high power sides were primarily functions of the instantaneous power flowing through the components on the corresponding side. The loss in the flywheel was mainly a function of its rotational speed, and thereby the instantaneous stored kinetic energy. To predict the aggregated loss in the complete system for a given drive-cycle, the associated losses in the three parts needed to be estimated.

To this end, a theoretical framework was compiled, permitting an exact analysis of measured data in such a system. Loss mechanisms both in power electronics as well as in the electric machine were described in detail. The study found that through a thorough understanding of the basic physical

processes in each component, a detailed separation of power-loss could be achieved, even though the individual loss factors could not be directly measured.

Drag losses due to air friction was found to be a dominating loss factor in the flywheel, increasing with rotational velocity to the power of 2.5. An estimate of the dimensionless roughness factor k_f of 2.3 ± 0.3 was deduced from the measurements. Further, a clear linear dependence on filling pressure was measured.

A separation of the remaining losses was possible by utilizing theoretical knowledge of the rotational dependency of the loss mechanisms. The separation yielded an estimate of the resistivity of the conductors perpendicular to their length, ρ_t , of $2.5 \times 10^{-8} \pm 3.5 \times 10^{-9}$, significantly higher than the nominal value of copper at 20 °C of 1.68×10^{-8} .

The machine losses were found to be dominating in the system. They comprised mechanical losses in the bearings, drag losses from air friction and eddy current losses in the windings of the electric machine. Future work includes reducing the losses by adding magnetic bearings to the system and replacing the stator windings with Litz wire. A reduction of eddy current loss with at least an order of magnitude should be possible since Litz wire typically has insulated strands with diameters of 0.2 mm.

References

1. Simonsen, M.; Walnum, H.J. Is the electric vehicle an attractive option for customers? *Energies* **2012**, *5*, 71–91.
2. García, I.; Miguel, L.J. Energy chain analysis of passenger car transport. *Energies* **2011**, *4*, 324–351.
3. Linden, D.; Reddy, T.B. *Handbook of Batteries*, 3rd ed.; McGraw-Hill: New York, NY, USA, 2002; p. 19.
4. Mellor, P.H.; Schofield, N.; Howe, D. Flywheel and supercapacitor peak power buffer technologies. In *Proceedings of the IEE Seminar on Electric, Hybrid and Fuel Cell Vehicles*, Durham, UK, 2010; Article 50, pp. 47–52.
5. Van Mierlo, J.; van den Bossche, P.; Maggetto, G. Models of energy sources for EV and HEV: Fuel cells, batteries, ultracapacitors, flywheels and engine-generators. *J. Power Sources* **2004**, *128*, 76–89.
6. Bolund, B.; Bernhoff, H.; Leijon, M. Flywheel energy and power storage systems. *Renew. Sustain. Energy Rev.* **2007**, *11*, 235–258.
7. Santiago, J.; Oliveira, J.G.; Lundin, J.; Abrahamsson, J.; Larsson, A.; Bernhoff, H. Design parameters calculation of a novel driveline for electric vehicles. *World Electr. Veh. J.* **2009**, *3*, 1–8.
8. Lundin, J. Flywheel in an All-Electric Propulsion System. Licentiate's Thesis, Uppsala University, Uppsala, Sweden, May 2011.
9. Lundin, J.; Oliveira, J.G.; Boström, C.; Yuen, K.; Kjellin, J.; Rahm, M.; Bernhoff, H.; Leijon, M. Dynamic Stability of an Electricity Generation System Based on Renewable Energy. In *Proceedings of the 21st International Conference on Electricity Distribution (CIRED 2011)*, Frankfurt, Germany, 6–9 June 2011.
10. Oliveira, J.G. Power Control Systems in a Flywheel based All-Electric Driveline. Ph.D. Thesis, Uppsala University, Uppsala, Sweden, August 2011.

11. Abrahamsson, J.; de Santiago, J.; Oliveira, J.G.; Lundin, J.; Bernhoff, H. Prototype of Electric Driveline with Magnetically Levitated Double Wound Motor. In *Proceedings of the XIX International Conference on Electrical Machines (ICEM)*, Rome, Italy, 6–8 September 2010.
12. Mohan, N.; Undeland, T. M.; Robbins, W.P. *Power Electronics Converters*, 2nd ed.; John Wiley & Sons: Hoboken, NJ, USA, 1995.
13. Pathak, A.D. *MOSFET/IGBT Drivers: Theory and Applications*; IXYS, Application note; IXYS Corporation: Santa Clara, CA, USA, 2002.
14. Carter, G.W. *The Electromagnetic Field in its Engineering Aspects*; Longmans: Harlow, UK, 1954; pp. 254–256.
15. Xu, T.; Sullivan, C.R. Stranded Wire with Uninsulated Strands as a Low-Cost Alternative to Litz Wire. In *Proceedings of Power Electronics Specialist Conference*, Acapulco, Mexico, 15–19 June 2003.
16. Palmgren, A. *Ball and Roller Bearing Engineering*, 3rd ed.; SKF Industries: Gothenburg, Sweden, 1959.
17. Lundberg, G., Palmgren, A. Dynamic capacity of rolling bearings. *Acta Polytech.* **1947**, *1*, 3.
18. Harris, T.A.; Kotzalas, M.N. Ball and Roller Loads Due to Bearing Applied Loading. In *Essential Concepts of Bearing Technology*, 5th ed.; CRC Press: Boca Raton, FL, USA, 2007; Chapter 10.
19. SKF. *SKF General Catalogue*; SKFAB: Gothenburg, Sweden, 2003; pp. 90–97.
20. Harris, T.A.; Kotzalas, M.N. Bearing Loads and Speeds. In *Essential Concepts of Bearing Technology*, 5th ed.; CRC Press: Boca Raton, FL, USA, 2007; Chapter 4.2.5.
21. Theodorsen, T.; Regier, A. Experiments of drag of revolving disks, cylinders, and streamline rods at high speeds. In *Thirtieth Annual Report of the National Advisory Committee for Aeronautics (NACA)*; Technical Report No. 793; NACA: Washington, DC, USA, 1944; pp. 367–384.
22. Larjola, J.; Sallinen, P.; Lindgren, O.; Esa, H.; Pyrhönen, J.; Lattu, J.; Falck, R. Basic research in high-speed technology. In *Lappeenranta University of Technology*; Technical Report EN B-71; Lappeenranta University of Technology: Lappeenranta, Finland, 1991; p. 185.
23. Pyrhonen, J.; Jokinen, T.; Hrabovcova, V. *Design of Rotating Electrical Machines*, 1st ed.; John Wiley & Sons: Hoboken, NJ, USA, 2008; p. 461.
24. Saari, J. Thermal Analysis of High-Speed Induction Machines. Ph.D. Thesis, Helsinki University of Technology, Espoo, Finland, 1998.
25. Daily, J.W.; Nece, R.E. Chamber dimension effects on induced flow and frictional resistance of enclosed rotating disks. *J. Basic Eng.* **1960**, *82*, 217–232.
26. SKF Homepage. Available Online: <http://www.skf.com> (accessed on 24 July 2012).